Influence of Particle Anisotropy and Motility on Preferential Concentration in Turbulence

Cristian Marchioli[1,2(✉)], Harshit Bhatia[1], and Diego Dotto[1]

[1] DPIA, University of Udine, 33100 Udine, Italy
marchioli@uniud.it
[2] International Center of Mechanical Sciences, 33100 Udine, Italy

Abstract. The simplest numerical framework to study turbulent particle dispersion assumes that particles can be modeled as point-like spheres brought about by the flow. In spite of its simplicity, this framework has led to significant advancements in the study of particle-turbulence interactions. In this paper we examine how particle dispersion in dilute turbulent suspensions changes when particles are non-spherical (elongated) and may actively move within the fluid (motile). In particular, we show how elongation and motility add to particle inertia to modulate preferential concentration. Results for particles suspended in wall-bounded turbulence are presented to highlight effects on wall accumulation and segregation, which represent the macroscopic manifestation of preferential concentration.

Keywords: Preferential concentration · Non-sphericity · Motility

1 Introduction

Particle transport in turbulent flows is fundamental to science and technology. Examples of open scientific issues include emissions reduction in combustion, rheological characterization of fibrous particle suspension, plankton population dynamics and convection of pollutants in the atmosphere. From a physical standpoint, whichever the flow geometry, particle dynamics is controlled by turbulent flow structures whose timescale is comparable to the particle Stokes number, defined as $St = \tau_p/\tau_f$ where τ_p is the characteristic relaxation time of the particle and τ_f is the characteristic time of the flow. Previous works focusing on turbulent dispersed flows in channels, pipes and jets (see [1,22] and references therein) show a strong correlation between coherent wall structures, local particle segregation and subsequent deposition and re-entrainment, the Stokes number being the scaling parameter. The reader is referred to [22] for an extensive review of these processes, how they are generated by particle-turbulence interactions at the particle scale and how they can be investigated by means of point-particle Euler-Lagrange simulations when particles are, in size, smaller than the Kolmogorov length scale of the flow. Here, we just provide a representative view of

M. Deville et al. (Eds.): TI 2018, NNFM 149, pp. 52–65, 2021.
https://doi.org/10.1007/978-3-030-65820-5_5

particle dynamics and distribution in a turbulent boundary layer, resulting from local microscopic particle-turbulence interactions in the dilute regime. Figure 1(a) shows a cross-sectional view of the instantaneous particle distribution in turbulent channel flow, obtained from point-particle direct numerical simulations in the absence of gravitational settling and assuming that particle dynamics is governed by the drag force only. The shear Reynolds number is $Re_\tau = 300$, based on the half channel height, and spherical particles with Stokes number $St = 30$ are considered. Particles appear non-homogeneously distributed across the channel, and tend to cluster. From these clusters, particles are transported to the wall, and accumulate in specific "reservoirs" where concentration build-up occurs. Particles tend to stay long times in these accumulation regions, classified by a streamwise velocity lower than the mean [20], so that eventually particle concentration increases near the wall. To quantify near-wall accumulation, in Fig. 1(b) we show the particle concentration, C/C_0 (namely, the number of particles counted per unit fluid volume, normalised by its initial value C_0), as a function of the non dimensional distance from the wall, z^+. Superscript + rep-

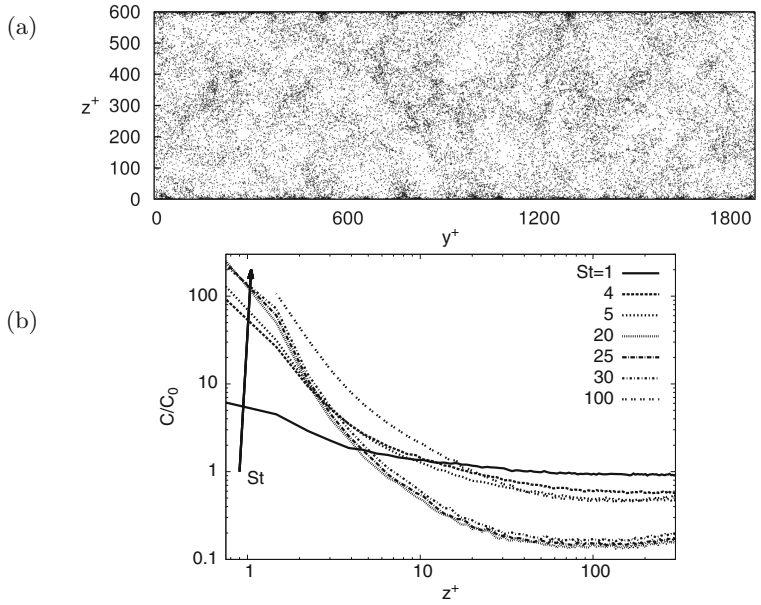

Fig. 1. Instantaneous distribution and wall accumulation of inertial particles in turbulent channel flow ($Re_\tau = 300$). Panels: (a) $St = 30$ particle position in the cross-flow plane; (b) particle concentration in the wall-normal direction, z^+. Concentration is computed as follows: (1) the flow domain is divided into N_s wall-parallel fluid slabs of variable thickness, $\Delta z^+(s)$ (using hyperbolic-tangent binning with stretching factor $\gamma = 1.7$); (2) the number $N_{p,s}$ of particles with center of mass located in the s^{th} slab at each time step is counted; (3) the number density $C = N_{p,s}/V_s$ is computed, with V_s the volume of the s^{th} slab. The normalized concentration is obtained dividing C by its initial value C_0.

resents wall units, defined in Sect. 2. Details on the calculation of C/C_0 can be found in [15]. The concentration profile corresponding to the $St = 30$ particle distribution of Fig. 1(a) is shown together with the profiles of additional particle sets, characterized by Stokes numbers ranging from 1 (relatively low inertia) to 100 (relatively high inertia). All concentration profiles develop a maximum well into the viscous sublayer, and the peak of C/C_0 increases monotonically with St, namely with particle inertia. This behaviour can be viewed as the outcome of the turbulence inhomogeneity [21].

Figure 1 provides an at-a-glance rendering of preferential concentration effects in a simplified and well-controlled situation in which these phenomena are due solely to particle inertia. Inertia introduces a time lag (the relaxation time, τ_p) in the particle response to the fluid velocity fluctuations. This leads to a deviation of particle trajectory with respect to pure tracers, which follow exactly the fluid streamlines. The ability to depart from fluid streamlines generates small-scale clustering and wall accumulation phenomena, explaining the fundamental physical mechanism by which a dilute suspension of inertial particles cannot be fully mixed by turbulence. In this paper, we investigate preferential concentration effects in more complex situations, characterized either by multiple sources of particle dispersion modulation, as in the case of heavy non-spherical particles, or by non-inertial effects, as in the case of motile particles that exploit their self-propelling capability to escape fluid streamlines. In both cases, we focus our discussion on dilute suspensions of point-wise particles and we exploit an Eulerian-Lagrangian approach based on direct numerical simulations of turbulence to examine statistically preferential concentration.

2 Methodology

The carrier fluid is Newtonian (with dynamic viscosity μ and kinematic viscosity ν) and incompressible (with density ρ). The fluid motion is governed by the following dimensionless mass and momentum conservation equations:

$$\nabla \cdot \mathbf{u} = 0; \qquad \dot{\mathbf{u}} + (\mathbf{u} \cdot \nabla)\mathbf{u} = -\nabla p + Re_\tau^{-1} \nabla^2 \mathbf{u} \tag{1}$$

where $\mathbf{u} = (u_x, u_y, u_z)$ is the fluid velocity, $\dot{\mathbf{u}}$ its time derivative, p is the fluid pressure, and $Re_\tau = hu_\tau/\nu$ is the shear Reynolds number, with h the channel half-height, and $u_\tau = \sqrt{\tau_w/\rho}$ the wall-friction velocity based on the wall shear stress τ_w. The flow is driven by a constant mean pressure gradient and is unaffected by the presence of the particles (one-way coupling). We performed direct numerical simulation of Eq. (1), considering both closed channel flow (for the spherical and elongated particles) and open channel flow (for the motile particles). Regardless of the flow configuration, periodic boundary conditions were imposed in the streamwise (x) and spanwise (y) directions. In the wall-normal/vertical direction (z), no-slip conditions at both walls were imposed in the closed channel configuration, whereas a free-slip condition was imposed at the free surface in the open channel configuration. Equations (1) are discretized using a pseudo-spectral method based on transforming variables into the wavenumber

space, through a Fourier representation in x and y, and a Chebyshev representation in z. A two-level explicit Adams-Bashforth scheme for the non-linear terms and an implicit Crank-Nicolson method for the viscous terms are employed for the time advancement. The convective non-linear terms are first computed in the physical space and then transformed in the wavenumber space using a de-aliasing procedure based on the 2/3-rule; derivatives are evaluated in the wavenumber space to maintain spectral accuracy [15].

Spherical particles with density $\rho_p >> \rho$ are injected into the flow at concentration low enough to consider dilute system conditions (particle-particle interactions are neglected). Particles are assumed to be pointwise, rigid and heavy, so that the most significant force acting on them is Stokes drag. To keep the simulation setting as simplified as possible, thus allowing direct comparison among the different types of inertial particles considered in this paper, the effect of gravity has also been neglected. With the above assumptions the following Lagrangian equation for the particle velocity is obtained [17]:

$$\dot{\mathbf{u}}_p = -0,75\,(C_D/d_p)\,(\rho/\rho_p)\,|\mathbf{u}_p - \mathbf{u}_{f@p}|(\mathbf{u}_p - \mathbf{u}_{f@p}), \tag{2}$$

with $\mathbf{u}_p = \dot{\mathbf{x}}_p$ the translational particle velocity, $\dot{\mathbf{u}}_p$ its time derivative, $\mathbf{u}_{f@p}$ the fluid velocity at the particle location, d_p the particle diameter, $C_D = 24Re_p^{-1}(1 + 0.15Re_p^{0.687})$ the drag coefficient, and $Re_p = d_p|\mathbf{u}_p - \mathbf{u}_{f@p}|/\nu$ the particle Reynolds number. For the present simulations, several particle sets were considered, characterized by different values of the relaxation time $\tau_p = \rho_p d_p^2/18\mu$, which is made dimensionless using wall variables and the Stokes number for each particle set is obtained as $St = \tau_p/\tau_f$ where $\tau_f = \nu/u_\tau^2$ is the characteristic flow time scale.

Elongated particles (also injected in a dilute flow, and referred to as fibers hereinafter) are modelled as pointwise rigid prolate spheroids with semi-major axis b, semi-minor axis a and aspect ratio $\lambda = b/a$. Translation and rotation are governed by the following equations:

$$m_p\dot{\mathbf{u}}_p = \mathbf{F}_D, \qquad (\mathbf{I}\cdot\dot{\boldsymbol{\omega}}') + \boldsymbol{\omega}' \times (\mathbf{I}\cdot\boldsymbol{\omega}') = \mathbf{M}', \tag{3}$$

where $m_p = 4\pi a^3\lambda\rho_p/3$ is fiber mass. In Eq. (3), $\mathbf{F}_D$ is the drag force acting on the fiber formulated in the *inertial* frame of reference $\mathbf{x} = \langle x, y, z\rangle$, $\mathbf{I}$ is the moment of inertia tensor, $\boldsymbol{\omega}'$ is the angular velocity of the fiber and $\mathbf{M}'$ is the Jeffery torque [6]. Both $\boldsymbol{\omega}'$ and $\mathbf{M}'$ are formulated in the *particle* frame of reference $\mathbf{x}' = \langle x', y', z'\rangle$ with origin at the fiber center of mass and axes x', y' and z' aligned with the principal directions of inertia. In the point-particle limit, the surrounding flow can be considered Stokesian and the drag force $\mathbf{F}_D$ can be expressed as [2]:

$$\mathbf{F}_D = \mu\mathbf{R}\mathbf{K}'\mathbf{R}^T \cdot (\mathbf{u}_{f@p} - \mathbf{u}_p) = \mu\mathbf{K} \cdot \Delta\mathbf{u} \tag{4}$$

where $\mathbf{R}$ is the orthogonal transformation matrix which relates the same vector in the two above-mentioned frames through the linear transformation $\mathbf{x} = \mathbf{R}\ \mathbf{x}'$ ($\mathbf{R}^T$ being its transpose), $\mathbf{K}'$ is the resistance tensor in the particle frame, and

$\Delta\mathbf{u} = \mathbf{u}_{f@p} - \mathbf{u}_p$ is the relative velocity between the fluid and the fiber at the center of mass of the fiber. Equation (4) is valid for a spheroid with arbitrary shape under creeping flow conditions, namely small fiber Reynolds number, $Re_p = 2a \mid \Delta\mathbf{u} \mid /\nu$. This condition is met for all fibers except the longest ones (see [23] for a more detailed discussion on the validity of the small-Re_p assumption for spheroids). The particle Stokes number is defined as [14]:

$$St = 4/3\,(\rho_p/\rho_f)\,(a^+)^2\lambda f(\lambda), \qquad f(\lambda) = \ln(\lambda + \sqrt{\lambda^2-1})/6\sqrt{\lambda^2-1}, \tag{5}$$

where superscript + indicates wall units, obtained using u_τ and ν ($a^+ = au_\tau/\nu$).

Motile particles (referred to as swimmers hereinafter) are modelled as massless pointwise sphere with position $\mathbf{x}_p$ evolving in time according to:

$$\dot{\mathbf{x}}_p(t) = \mathbf{u}_{f@p}(\mathbf{x}_p) + v_s\mathbf{p}, \tag{6}$$

where v_s is the (constant) swimming speed, and the unit vector $\mathbf{p}$ defines the spatial orientation of the swimmer. Vector $\mathbf{p}$ evolves in time according to the response of the swimmer to the biasing torques acting upon it: The viscous torque caused by shear, which rotates the body according to the local velocity gradients, and the gyrotactic torque arising from bottom heaviness, which tends to align the swimmer along the vertical direction $\mathbf{k}$ [19]. The orientation rate is computed as:

$$\dot{\mathbf{p}} = (2\mathcal{B})^{-1}\,[\mathbf{k} - (\mathbf{k}\cdot\mathbf{p})\mathbf{p}] + \omega_{f@p} \wedge \mathbf{p} \tag{7}$$

with $\mathbf{k}$ the unit vector pointing upward in the vertical direction, $\omega_{f@p}$ the fluid vorticity at the swimmer's position, and $\mathcal{B}$ the characteristic time a perturbed gyrotactic swimmer takes to re-orient vertically when $\omega_{f@p} = 0$. The first term on the rhs of Eq. (7) represents the tendency of a swimmer to remain aligned with the vertical direction due to bottom-heaviness, while the second term represents the tendency of fluid vorticity to overturn the swimmer through a viscous torque. The key parameters in Eqs. (6) and (7) are the stability number $\Psi = \frac{1}{2\mathcal{B}}\frac{\nu}{u_\tau^2}$, which parameterises the importance of vortical overturning with respect to directional swimming, and the swimming number $\Phi = v_s/u_\tau$. As done for the inertial particles, swimmers are tracked assuming dilute flow conditions and using a point-particle approach, justified by the sub-Kolmogorov size typical of aquatic micro-organisms.

The statistics presented in this paper are relative to a turbulent Poiseuille channel flow. For the spherical and elongated particles, the shear Reynolds number is $Re_\tau = 300$, corresponding to a bulk Reynolds number $Re = u_0 h/\nu = 4200$, with $u_0 \simeq 3.3\ m/s$ (resp. $u_0 \simeq 0.21\ m/s$) the bulk velocity in the case of gas-solid flow (resp. liquid-solid flow). For the swimmers, values of Re_τ from 170 to 1020 were considered in order to explore Re_τ effects on vertical migration dynamics. In all simulations, and regardless of the specific value of Re_τ, the domain size is $L_x \times L_y \times L_z = 4\pi h \times 2\pi h \times 2h$ in the streamwise, spanwise and wall normal/vertical directions, respectively. The grids used to discretize this domain are given in Table 1. Lagrangian tracking of inertial particles was performed considering both spherical particles with Stokes numbers ranging from $St = 1$

to $St = 100$, and fibers with Stokes numbers $St = 5$ and $St = 30$ and aspect ratio $\lambda = 3, 10, 50$ (the case $\lambda = 1$ was also considered, to allow comparison with spherical particles). The simulation parameters for the different particle sets are provided in Tables 2 and 3, respectively. To simulate the motion of the swimmers, we fixed $\Phi = 0.048$, corresponding to a dimensional swimming velocity $v_s = 100$ $\mu m/s$ typical of *Chlamydomonas augustae* [4], and varied the stability number ($\Psi_H = 1.13$, $\Psi_I = 0.113$, $\Psi_L = 0.0113$), corresponding to $\mathcal{B} = 0.054, 0.54$ and 5.4 s, respectively: These values fall within the typical range of motile phytoplankton species [4].

Table 1. Simulation parameters for the flow field.

Flow configuration	Shear Reynolds number, Re_τ	Grid points $N_x \times N_y \times N_z$	Shear velocity u_τ $[m\ s^{-1}]$	Bulk Reynolds number, Re_b
Closed channel	300	$256 \times 256 \times 257$	0.2355	4200
Open channel	170	$128 \times 128 \times 129$	0.006	1400
	510	$256 \times 256 \times 257$	0.018	4300
	1020	$512 \times 512 \times 513$	0.036	8600

Table 2. Spherical particles simulation parameters (closed channel flow, $Re_\tau = 300$). V_s^+ is the dimensionless terminal velocity of the particle in still fluid.

St	τ_p (s)	d_p^+	d_p (μm)	$V_s^+ = g^+ \cdot St$	$Re_p^+ = V_s^+ \cdot d_p^+ / \nu^+$
1	$0.283 \cdot 10^{-3}$	0.153	10.2	0.0118	0.00275
4	$1.132 \cdot 10^{-3}$	0.306	20.4	0.0472	0.01444
5	$1.415 \cdot 10^{-3}$	0.342	22.8	0.0590	0.02018
20	$5.660 \cdot 10^{-3}$	0.684	45.6	0.2358	0.16129
25	$7.075 \cdot 10^{-3}$	0.765	51.0	0.2948	0.22552
100	$28.30 \cdot 10^{-3}$	1.530	102.0	1.1792	1.80418

Table 3. Elongated particles simulation parameters (closed channel flow, $Re_\tau = 300$).

St	Shape	λ	ρ_p/ρ_f	ρ_p	$2b^+$	$2b$ (μm)	-	St	Shape	λ	ρ_p/ρ_f	ρ_p	$2b^+$	$2b$ (μm)
5	Sphere	1	173.6	225.7	0.72	96.07	-	30	Sphere	1	1041.7	1354.2	0.72	96.07
5	Ellipsoid	3	92.9	120.8	2.16	287.9	-	30	Ellipsoid	3	557.1	724.2	2.16	287.9
		10	57.7	75	7.2	960.1				10	346.3	450.2	7.2	960.1
		50	37.7	49	36	4800				50	226.2	294	36	4800

For each tracked set, $N_p = 10^6$ particles/swimmers were injected into the flow with random position, random orientation and velocity equal to the fluid velocity at the release position. The equations of motion were solved using a 4^{th} order Runge-Kutta scheme with a time step equal to that of the fluid. The fluid velocity and vorticity at the instantaneous particle location were obtained through interpolation based on 6th-order Lagrange polynomials. Periodic boundary conditions were imposed on particles in both streamwise and spanwise directions, whereas elastic reflection and conservation of angular momentum were applied when a particle touched the wall (or the free surface, in the case of the microswimmers). Elastic reflection was chosen since it is the most conservative assumption when measuring preferential concentration in a turbulent boundary layer. A more detailed discussion on the modelling issues associated to particle-wall collisions, not included here for sake of brevity, can be found in [16,23].

3 Results and Discussion

We discuss the effect on preferential concentration introduced by two properties that provide particles with the ability to escape fluid streamlines: Particle shape (elongation, in particular, which adds to inertia in our problem) and particle motility (which leads to particle non-homogeneous distribution even without inertia). Statistics presented in this section were computed starting at time $t^+ = 1000$ upon particle injection, and gathered for a span $\Delta t^+ = 2000$, unless otherwise indicated.

Effect of Elongation on Preferential Concentration
Figure 2 shows the instantaneous distribution of the $St = 30$ fibers with $\lambda = 10$ (taken here as reference for the visualization) in the center region (panel a)

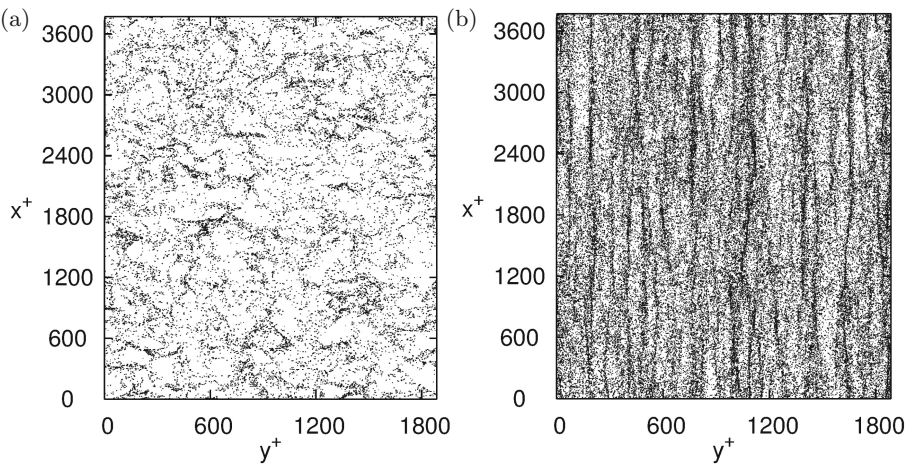

Fig. 2. Spatial distribution of $St = 30$ fibers with $\lambda = 10$ in closed channel flow at $Re_\tau = 300$. Panels: (a) Channel center; (b) Near-wall region.

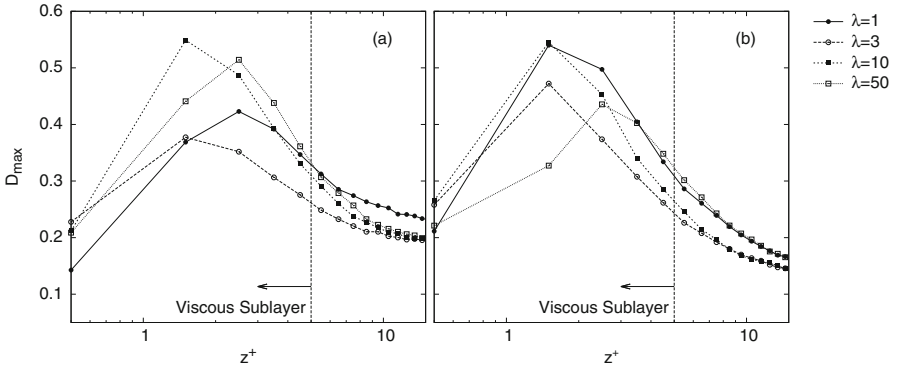

Fig. 3. Segregation parameter, D_{max}, along the wall-normal direction for inertial elongated fibers in closed channel flow at $Re_\tau = 300$. Panels: (a) $St = 5$; (b) $St = 30$.

and in the near-wall region (panel b) of the channel. Similar distributions are observed for the other sets (not shown). In the channel center, fibers cluster into groups leaving empty regions that have the same location for all fiber sets. This indicates that, in spite of the strong mathematical coupling between rotational and translational equations due to the dependency of the resistance tensor on the orientation [13], macroscopic fiber distributions are unaffected by elongation and depend only on inertia. Near the wall, fibers segregate into elongated streaks that correlate with regions of low-speed fluid velocity, but do not exhibit a strong preferential orientation in the streamwise direction. To examine in a more quantitative way the relative tendency of fibers to segregate in a turbulent flow, we computed the deviation from randomness, $D \equiv (\sigma - \sigma_{Poisson})/\mu$ [5], where σ is the standard deviation for the measured number density distribution, $\sigma_{Poisson}$ is the standard deviation for a Poisson distribution (i.e. a purely random distribution of the same number of particles), and μ is the mean particle number density. $D = 0$ corresponds to a random distribution, $D < 0$ corresponds to a uniform distribution, $D > 0$ indicates segregation (larger values of D correspond to stronger segregation). The value calculated for D depends on the size of the cell volume Ω_{cell} used for the calculation. This dependency can be partially overcome by computing the number density distribution for several values of Ω_{cell} and keeping only the largest value of D [20], indicated as D_{max} in the following. In Fig. 3, we show the behavior of D_{max} as a function of the wall-normal coordinate, z^+, for all cases considered in the (λ, St)-space. Profiles are averaged both in space, over the homogeneous directions, and in time, over the last 200 time units of the simulations. Segregation reaches a maximum inside the viscous sublayer ($z^+ < 5$), suggesting that such build-up is driven by inertia. Indeed, the larger values of D_{max} are obtained for the $St = 5$ and $St = 30$ fibers, which exhibit the highest tendency to undergo low-speed streak segregation. Small values are obtained for the $St = 1$ fibers, which exhibit the lowest tendency to undergo low-speed streak segregation (not shown), in agreement

with previous findings [14]. Once in the viscous sublayer, however, elongation becomes important in determining the location and the magnitude of maximum segregation. Changes in the aspect ratio produce non-monotonic modifications and cross-overs between profiles indicating that, locally, the influence of wall turbulence on fibers is strongly affected by λ and not only by St.

The results in Fig. 3 indicate the presence of a specific parameter range in which inertia combines with elongation to give rise to a non-trivial behaviour eventually leading to significant quantitative changes in near-wall dispersion. These will be analyzed next by means of concentration statistics. Figure 4 shows the instantaneous concentration profiles, computed as in [14], for both $St = 5$ fibers (panel a) and $St = 30$ fibers (bottom panel). The most evident changes occur in the very near-wall region, within few wall units from the wall: each profile develops a peak of concentration which is always found within the closest fluid slab considered for fiber counting. The peak value of C/C_0 differs depending on the aspect ratio: Compared to the spherical particles (black circles) with the same Stokes number, we observe a sharp increase of fiber accumulation already at $\lambda = 3$ for $St = 5$, followed by a decrease for longer fibers. Figure 4(b) suggests that this effect fades away for the shortest fibers ($\lambda < 10$ in our simulations) as fiber inertia increases. We remind that, for a given value of St, the mass of a fiber increases with its elongation so longer fibers have higher inertia. Therefore, the modification of the statistics that we observe when we increase the aspect ratio is due to a change in particle shape and is both direct and indirect (through increased inertia). Outside the viscous sublayer, variations are less evident and, again, the elongation of the fiber does not seem to play an important role. Overall, the results just discussed indicate that the fiber responsiveness to segregation and preferential concentration induced by the flow is strongly (and directly) correlated to the fiber aspect ratio mostly in the viscous sublayer, where particle anisotropy due to non-sphericity adds to flow anisotropy and the combined effects of shape and inertia lead to a quantitatively different build-up of fibers.

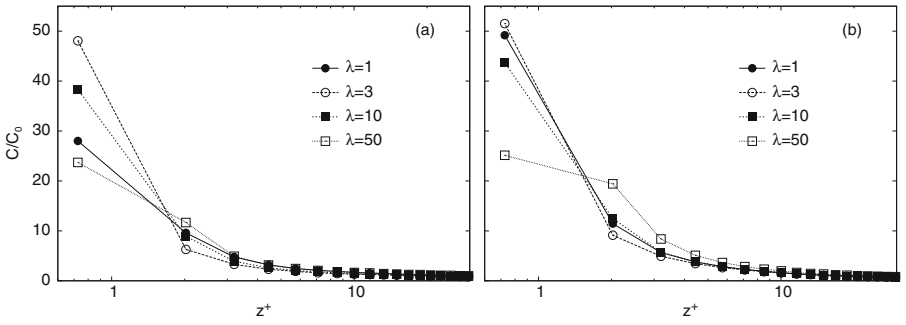

Fig. 4. Fiber concentration in the wall-normal direction (closed channel flow, $Re_\tau = 300$. Panels: (a) $St = 5$; (b) $St = 30$. Concentration was computed as explained in Fig. 1.

Effect of Motility on Preferential Concentration

A physical problem in which preferential concentration is observed in the absence of inertia is provided by the rising of gyrotactic micro-swimmers in free-surface turbulence. This phenomenon has been investigated recently [10,11,16], with the aim of elucidating the importance of the swimmer's vertical stability on its ability to move through turbulent vortices and reach the sub-surface layers of the flow. Turbulent flow structures near the free surface have been widely investigated [7,18]. Within the range of Re_τ investigated here, surface structures are generated and sustained by bursting phenomena that are continuously produced by wall shear turbulence inside the buffer layer. Bursts emanate from the bottom of the channel and produce upwelling motions of fluid that are advected toward the free surface. Near the surface, turbulence is restructured due to damping of vertical fluctuations: upwellings appear as sources for the surface-parallel fluid velocity and alternate to sinks associated with fluid downdrafts from the surface to the bulk. This phenomenology has been long recognized to produce flow with properties that differ from those typical of 2D incompressible turbulence [9]. To characterize the surface topology, we use the surface divergence $\nabla_{2D} = \frac{\partial u_f}{\partial x} + \frac{\partial v_f}{\partial y} = -\frac{\partial w_f}{\partial z}$. In open channel flow, ∇_{2D} does not vanish and swimmers located on the free surface probe a compressible 2D system [3], where velocity sources are regions of local flow expansion ($\nabla_{2D} > 0$) generated by upwellings and velocity sinks are regions of local compression ($\nabla_{2D} < 0$) due to downwellings. Figure 5 provides a qualitative characterization of swimmer clustering on the free surface by correlating the instantaneous swimmer distribution with the colormap of ∇_{2D}. Due to gyrotaxis, swimmers can not retreat from the free surface by simply following flow motions: They can only leave velocity sources (red areas in Fig. 5) and collect into velocity sinks (blue areas in Fig. 5), where they organize themselves in clusters that are stretched by the fluid to form filamentary structures. Formation of clusters with fractal mass distribution has been observed previously for the case of Lagrangian tracers in surface flow turbulence without mean shear [3,8], with wind-induced shear [16], and for the case of floaters in free-surface turbulence [11].

Another feature of swimmer dynamics that is clearly highlighted in Fig. 5, is the different number of cells that have reached the surface at the time instant of the visualizations. Swimmers with low gyrotaxis (low stability number Ψ_L, panel a), are out-numbered by swimmers with high gyrotaxis (high stability number Ψ_H, panel b). To quantify this qualitative observation, in Fig. 6(a) we show the wall-normal concentration profiles computed at the same time of Fig. 5 ($t^+ = 10^4$), comparing results at varying gyrotaxis. Concentration builds up within a thin layer just below the surface. The maximum value of concentration is reached right at the surface, and increases monotonically with gyrotaxis. In the bulk of the flow, the distribution of the swimmers remains uniform whereas the bottom wall is depleted of cells, indicating a continuous migration towards the free-surface. This process can be further analyzed considering the time behaviour of the number of swimmers that have reached the surface, represented by the solid line in Figs. 6(b)–(d), and normalized by the total number of swimmers

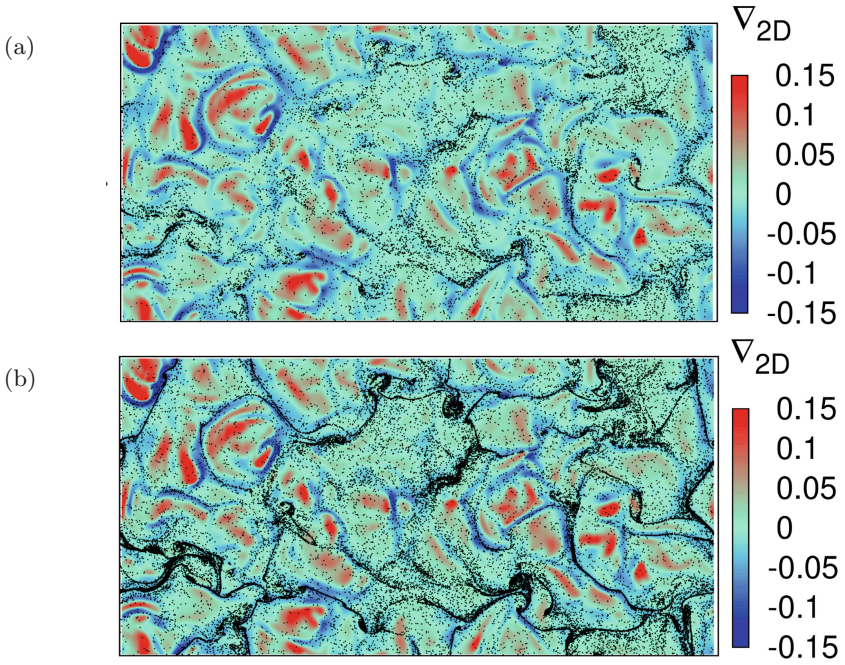

Fig. 5. Top view of micro-swimmers distribution on the free surface ($Re_\tau = 510$, $t^+ = 10^4$). Flow is from left to right. Panels: (a) Low gyrotaxis, Ψ_L; (b) High gyrotaxis, Ψ_H.

tracked in the simulations. More precisely, these figures show the number of swimmers trapped in a monitor fluid slab $0.01 < z^+ < 0.5$ just below the free-surface, chosen in order to minimise the effect of the elastic rebound condition imposed at the upper boundary of the flow domain. In addition, the dashed and dotted curves in each figure represent the fraction of swimmers located in regions of the monitor fluid slab characterized by negative and positive values of the surface divergence, respectively. In agreement with the qualitative observations drawn from Fig. 5, the number of swimmers sampling $\nabla_{2D} < 0$ in downwelling regions is always much higher than the number of swimmers sampling $\nabla_{2D} > 0$ in upwelling regions. Within the time window of the simulations, n/N reaches a steady state only for swimmers with low gyrotaxis, Ψ_L, and only $5 \sim 6\%$ of the swimmers are able to reach the surface. For the cases of intermediate and high gyrotaxis, n/N increases steadily (up to roughly 70% for the Ψ_I swimmers and roughly 80% for the Ψ_H swimmers), and provides the source for continuous accumulation into filamentary clusters within downwellings.

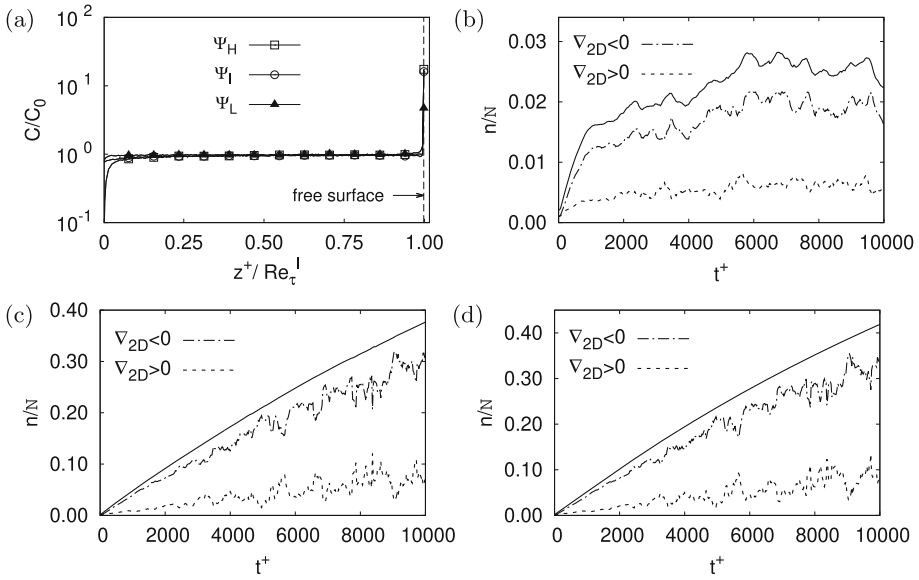

Fig. 6. Surfacing and accumulation of gyrotactic micro-swimmers ($Re_\tau = 510$). Panels: (a) Wall-normal concentration at varying gyrotaxis; (b), (c), (d) Evolution of the number of swimmers reaching the sub-surface layer $0.1 < z^+ < 0.5$ for low, intermediate and high gyrotaxis. The relative contributions due to swimmers in downwellings ($\nabla_{2D} < 0$, dash-dotted lines) and upwellings ($\nabla_{2D} > 0$, dashed lines) are also shown.

4 Conclusions

We have examined two instances of turbulent dispersed flow in which preferential concentration phenomena are not determined solely by particle inertia, and we have tried to highlight the differences introduced by the presence of shape effects or motility effects. The physical problems investigated all refer to one-way coupled flows, and therefore the results discussed in this paper are valid only for dilute particle suspensions. Our results show that, when shape effects add to inertial effects, significant quantitative modifications to particle segregation into clusters and to particle accumulation near solid boundaries occur. Such quantitative changes are, in general, not monotonically dependent on the increase of particle elongation and appear difficult to model within numerical approaches that are not based on direct numerical simulations of turbulence. In particular, it would be useful to include shape effects in subgrid closure models for predicting preferential concentration via Large-Eddy simulations [12]. However, present results suggest that this may be a very challenging task. We also show that preferential concentration can be observed in the absence of inertia, by considering particles that can propel themselves within the fluid. In this case, preferential

concentration is associated to two-dimensional clustering at a free surface, where the degree of segregation can be "tuned" by modulating the vertical stability of directional swimming.

References

1. Balachandar, S., Eaton, J.K.: Turbulent dispersed multiphase flow. Annu. Rev. Fluid Mech. **42**, 111–133 (2010)
2. Brenner, H.: The Stokes resistance of an arbitrary particle. Chem. Eng. Sci. **18**, 1–25 (1963)
3. Cressman, J.R., Davoudi, J., Goldburg, W.I., Schumacher, J.: Eulerian and Lagrangian studies in surface flow turbulence. New J. Phys. **6**, 53 (2004)
4. Durham, W.M., Climent, E., Barry, W.M., De Lillo, F., Boffetta, G., Cencini, M., Stocker, R.: Turbulence drives microscale patches of motile phytoplankton. Nat. Commun. **4**, 2148 (2013)
5. Fessler, J.R., Kulick, J.D., Eaton, J.K.: Preferential concentration of heavy particles in a turbulent channel flow. Phys. Fluids **6**, 3742–3749 (1994)
6. Jeffery, G.B.: The motion of ellipsoidal particles immersed in a viscous fluid. Proc. Roy. Soc. **102**, 161–179 (1922)
7. Kermani, A., Khakpour, H.R., Shen, L., Igusa, T.: Statistics of surface-renewal of passive scalars in free-surface turbulence. J. Fluid Mech. **678**, 379 (2011)
8. Larkin, J., Bandi, M.M., Pumir, A., Goldburg, W.I.: Power-law distributions of particle concentration in free-surface flows. Phys. Rev. E **80**, 066301 (2009)
9. Lovecchio, S., Zonta, F., Soldati, A.: Upscale energy transfer and flow topology in free surface turbulence. Phys. Rev. E **91**, 033010 (2015)
10. Lovecchio, S., Zonta, F., Soldati, A.: Influence of thermal stratification on the surfacing and clustering of floaters in free surface turbulence. Adv. Water Res. **72**, 22–31 (2014)
11. Lovecchio, S., Marchioli, C., Soldati, A.: Time persistence of floating particle clusters in free-surface turbulence. Phys. Rev. E **88**, 033003 (2013)
12. Marchioli, C.: Large-eddy simulation of turbulent dispersed flows: a review of modelling approaches. Acta Mech. **228**, 738–768 (2017)
13. Marchioli, C., Zhao, L., Andersson, H.I.: On the relative rotational motion between rigid fibers and fluid in turbulent channel flow. Phys. Fluids **28**, 013301 (2016)
14. Marchioli, C., Fantoni, M., Soldati, A.: Orientation, distribution and deposition of elongated, inertial fibers in turbulent channel flow. Phys. Fluids **22**, 033301 (2010)
15. Marchioli, C., et al.: Statistics of particle dispersion in direct numerical simulations of wall-bounded turbulence: results of an international collaborative benchmark test. Int. J. Multiphase Flow **34**, 879–893 (2008)
16. Mashayekhpour, M., Marchioli, C., Lovecchio, S., Nemati Lay, E., Soldati, A.: Wind effect on gyrotactic micro-organism surfacing in free-surface turbulence. Adv. Water Resour. **129**, 328–337 (2019)
17. Maxey, M., Riley, J.: Equation of motion for a small rigid sphere in a nonuniform flow. Phys. Fluids **26**, 883–889 (1983)
18. Nagaosa, R., Handler, R.A.: Statistical analysis of coherent vortices near a free surface in a fully developed turbulence. Phys. Fluids **15**, 375–394 (2003)
19. Pedley, T.J., Kessler, J.O.: Hydrodynamic phenomena in suspensions of swimming microorganisms. Annu. Rev. Fluid Mech. **24**, 313–358 (1992)

20. Picciotto, M., Marchioli, C., Soldati, A.: Characterization of near-wall accumulation regions for particles in turbulent boundary layers. Phys. Fluids **17**, 098101 (2005)
21. Reeks, M.W.: The transport of discrete particles in inhomogeneous turbulence. J. Aerosol Sci. **310**, 729–739 (1983)
22. Soldati, A., Marchioli, C.: Physics and modelling of turbulent particle deposition and entrainment. Int. J. Multiphase Flow **35**, 827 (2009)
23. Zhao, L., Marchioli, C., Andersson, H.I.: Slip velocity of rigid fibers in turbulent channel flow. Phys. Fluids **26**, 063302 (2014)